Supplementary Information for Long-range propagating paramagnon-polaritons in organic free radicals

Sebastian Knauer[1*], Roman Verba[2], Rostyslav O. Serha[1,3], Denys Slobodianiuk[2], David Schmoll[1,3], Andreas Ney[4], Sergej O. Demokritov[5], Andrii V. Chumak[1*]

[1]Faculty of Physics, University of Vienna, Vienna, 1090, Austria.
[2]V. G. Baryakhtar Institute of Magnetism of the NAS of Ukraine, Kyiv, 03142, Ukraine.
[3]Vienna Doctoral School in Physics, University of Vienna, Vienna, 1090, Austria.
[4]Institut für Halbleiter-und Festkörperphysik, Johannes Kepler Universität, Münster, 4040, Austria.
[5]Institute for Applied Physics, University of Münster, Münster, 48149, Germany.

*Corresponding author(s). E-mail(s): knauer.seb@gmail.com; andrii.chumak@univie.ac.at;

This PDF file includes:

Supplementary Text
Supplementary Figures 1 to 11

The supplementary information provides additional details, methods, and figures to support the main text's findings. This encompasses sample preparation, theoretical background, experimental setup, EPR, and propagating paramagnon measurements.

1 Sample preparation

Supplementary Figure 1 illustrates the process of fabricating and mounting the sample. We utilise commercially available 2,2,6,6-Tetramethylpiperidin-1-oxyl (TEMPO), which has a molecular weight of 156.25 g/mol and a purity greater than 97.5 %. The substance is heated to a constant temperature of 65°C until it becomes molten. Afterwards, we employ capillary forces to fill a capillary lab tube with the molten material; this tube has an inner diameter of 1.1 mm and an outer diameter of 1.5 mm and is approximately 15 mm long. Once filled, the tube ends are securely sealed to prevent leakage or contamination.

Then, the sample is mounted on a printed circuit board (PCB) equipped with two grounded microwave antennas for the continuous-frequency (cf) and pulsed (time-resolved) measurements. The antennas have a width of 25 μm, with spacings of 4 mm for continuous-frequency measurements and 8 mm for pulsed measurements. The PCB-sample setup, in combination with the cryogenic environment, enables the system to operate effectively at up to 40 GHz, ensuring high-precision measurements.

For the EPR measurements, the glass capillary sample is affixed to a high-frequency stripline PCB. The stripline PCB comprises a 200 μm coplanar waveguide (dielectric constant 3.26) with 150 μm spacing on either side to the ground line, and is matched to 50 Ω.

Only for the VSM measurement, a separate sample holder was built, see Supplementary Fig. 2. The sample holder is 3D-printed from non-magnetic resin and consists of a 2 mm-long hollow capillary (O.D. 5 mm, I.D. 3 mm) and a sealing cap. The capillary is filled with TEMPO (Supplementary Fig. 2 left). To measure the correct volume of TEMPO, the weight of the capillary and cap is recorded before and after filling with TEMPO. We use 1g/cm^3 as the density of TEMPO. The sealing cap closes the capillary (Supplementary Fig. 2 right). The cap is further secured with epoxy glue.

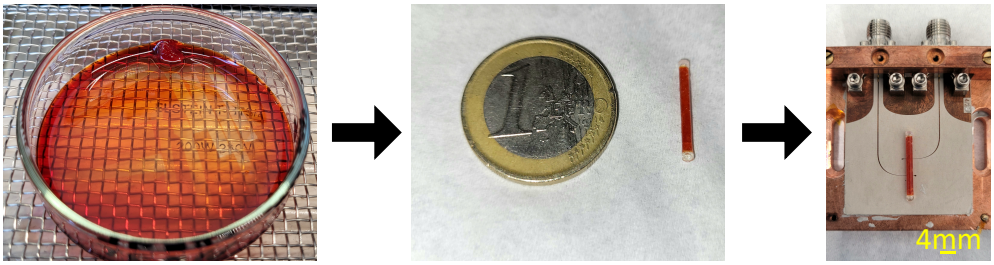

Fig. 1 Sample preparation. First, 2,2,6,6-Tetramethylpiperidin-1-oxyl is molten at a constant temperature of 65°C in a Petri dish on a hotplate. Then, capillary forces are used to fill capillary tubes (I.D. 1.1 mm, O.D. 1.5 mm, length about 15 mm). The ends of the capillary are sealed air-tight. Subsequently, the sample is mounted on a high-frequency PCB (see Supplementary Text).

Fig. 2 Sample holder for VSM measurements. Left: A sample holder is 3D-printed from non-magnetic resin and consists of a 2 mm long hollow capillary (O.D. 5 mm, I.D. 3 mm) and a sealing cap. The capillary is filled with TEMPO. To measure the correct volume of TEMPO, the weight of the capillary and cap is recorded before and after filling with TEMPO. We use $1 g/cm^3$ as the density of TEMPO. Right: Example of a closed VSM capillary. The cap is further secured with epoxy glue.

2 Theory

2.1 Temperature dependence of TEMPO magnetisation

In the manuscript's initial section, we explore how temperature affects the magnetisation of TEMPO (also see Fig. 1b-d). For an idealised paramagnet, we can use Brillouin's theory to evaluate TEMPO's magnetisation $M = M(B_e, T)$, using the modified implicit equation in Ref. [1]:

$$M = M_0 g \mu_\mathrm{B} J B_{1/2}(x), \tag{1}$$

where M_0 is the saturation magnetisation of TEMPO, $g = 2.0027$ the Landé factor, μ_B the Bohr magneton, $B_{1/2}$ the Brillouin function for the angular momentum $J = 1/2$, λ is the coefficient of molecular field, and μ_0 the vacuum magnetic permeability. The ratio of the Zeeman energy of the magnetic momentum in the external field to the thermal energy is represented by $x = Jg\mu_\mathrm{B}B/(k_\mathrm{B}T)$, where k_B is the Boltzmann constant and T is the temperature. For our investigations, we will omit all terms of demagnetisation, which will serve as the basis for future research. Thus we obtain

$$M = M_0 B_{1/2}\left(\frac{1}{2}\frac{g\mu_\mathrm{B}(B_\mathrm{e} + \lambda\mu_0 \cdot M)}{k_\mathrm{B}T}\right). \tag{2}$$

First, for near room temperature and high Kelvin temperatures, we also omit all the molecular field parameters. The results are shown in Supplementary Fig. 3

The data points are represented as dots, with the corresponding Brillouin fits depicted as color-coded lines. The optimal fit is determined at room temperature and 50 K for a magnetisation value of $M_0 = 25.5\,\mathrm{kA/m}$. At 10 K, however, the fit begins

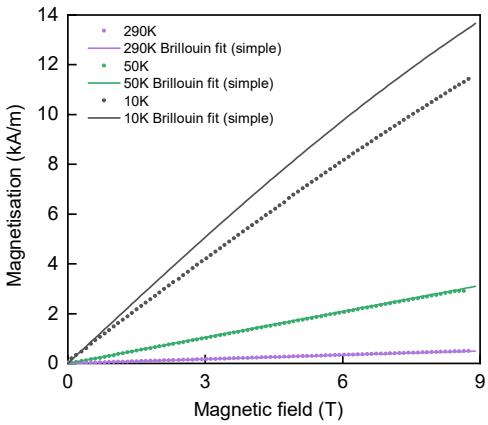

Fig. 3 Magnetisation of TEMPO with respect to the magnetic field for 290, 50, and 10 K, using vibrating sample magnetometry. The data points are dotted, and the corresponding Brillouin fits are lines (colour-coded). For these fits, we omit all demagnetisation and molecular field coefficients ($\lambda = 0$). We find the best fit at room temperature and 50 K for $M_0 = 25.5\,\mathrm{kA/m}$. At 10 K, the fit diverges from the data points, indicating that TEMPO undergoes a fundamental change in magnetisation and the paramagnetic moments start to interact. These are the first indications of magnetic order above the Néel temperature.

to diverge from the experimental data points, suggesting that TEMPO experiences a fundamental change in its magnetisation behaviour at this temperature. This observation shows that the magnetic ordering occurs well above the Néel temperature. Thus, we have to introduce an additional fit parameter (molecular field coefficient) to compensate for this effect in our fits.

Therefore, for our Brillouin fit of the 2 K data (see Fig. 1c main text, red), we use the experimentally obtained effective saturation magnetisation of $M_0 = 24\mathrm{kA/m}$ (see Fig. 1b main text) and keep the molecular field coefficient as a free fitting parameter, which gives us $\lambda \approx -183$. We observe good agreement between theory and experimental data at 2 K, allowing us to extrapolate the effective magnetisation at 50 mK (see Fig. 1c main text, blue).

For completeness, for 10 K we require $\lambda \approx -45$, and for 4 K $\lambda \approx -130$ in our fit function to overlap with our data.

2.2 Spin wave spectrum

Here, we present details of the spin-wave spectrum calculations used in the main text to estimate the expected velocity and delay of paramagnons. The spectrum of paramagnons is nothing but the spectrum of magnetostatic waves at given saturation magnetisation $M_s = M_s(T, B_e)$.

For the BV geometry (external field is aligned to the capillary axis), the problem of magnetostatic wave spectrum calculation can be solved semi-analytically [2, 3]. The

spectrum is determined from the following implicit expression:

$$\sqrt{-\mu}\frac{J'_m(\frac{kR}{\sqrt{-\mu}})}{J_m(\frac{kR}{\sqrt{-\mu}})} + \frac{m\mu_a}{kR} + \frac{K'_m(kR)}{K_m(kR)} = 0, \tag{3}$$

where k is the spin wave wave number, R is the capillary radius, J_m and K_m are Bessel and modified Bessel functions of the first and second kind, respectively, short notation $J'_m(x) \equiv (J_{m-1}(x) - J_{m+1}(x))/2$ stands for the Bessel function derivative (and the same for $K'_m(x)$), and components of relative permeability tensor are given as usual:

$$\mu = \frac{\omega_H(\omega_H + \omega_M) - \omega_k^2}{\omega_H^2 - \omega_k^2} - 1, \quad \mu_a = \frac{\omega_k\omega_M}{\omega_H^2 - \omega_k^2}. \tag{4}$$

Here, standard notation is used: $\omega_H = \gamma B_e$, $\omega_M = \gamma\mu_0 M_s$. The integer index m describes the azimuthal number of the magnetostatic wave mode. In our case, we are looking for modes that have a nonzero net dynamic magnetic moment and, thus, could be excited by RF antennas. These are modes with $m = -1$. Note that the azimuthal number in polar components, which is used in Supplementary Eq. 3, differs from the azimuthal number in Cartesian components by 1.

We have used the following parameters for spectrum calculation: $B_e = 500\,\mathrm{mT}$, $M_s = 2.2\mathrm{kA/m}$, $R = 650\,\mu\mathrm{m}$. Calculated dispersion relations of the three lowest-order modes are shown in Supplementary Fig. 4(a) by dashed lines. The whole spectrum lies in the range $\sqrt{\omega_H(\omega_H + \omega_M)} > \omega_k > \omega_H$, which, in our case, is only 50 MHz. There are also surface spin-wave modes in such a system [3], but their frequency lies much above the bulk mode spectrum, and we disregard them.

We also performed micromagnetic simulations using MuMax3 software [4]. A capillary of 160.7 mm length was discretised into $1024 \times 32 \times 32$ cells, which is enough to capture the necessary range of spin-wave spectrum. The exchange constant was set to $A_{ex} = 0$. Magnetisation dynamics was excited by a spatially-localised sinc-shape in time pulse, and the spin-wave spectrum was calculated by 2D time-space FFT of magnetisation dynamics, averaged over the capillary cross-section. For BV geometry, micromagnetic results agree nicely with the above theory, see Supplementary Fig. 4(a).

Micromagnetic simulation also allows for finding the spectrum for the case of a perpendicular applied field, which is not accessible with semi-analytic theory. In this case, magnetostatic waves are forward waves, and only the fundamental (quasiuniform) mode is clearly visible in the simulations (Supplementary Fig. 4(b)).

The group velocity of the fundamental mode at low k is $v_{gr} \approx 54\,\mathrm{km/s}$ for the field applied axially, and is $v_{gr} \approx 32\,\mathrm{km/s}$ for the perpendicularly magnetised case at $M_s = 2.2\,\mathrm{kA/m}$. In the range of interest, the group velocity scales linearly with TEMPO magnetisation.

2.3 Magnon-polariton spectrum estimation

Accurate calculation of magnon-polariton dispersion relation in cylindrical geometry is a cumbersome task, which can be solved only numerically. Instead, here we estimate magnon-polariton dispersion curve using an established approach from cavity

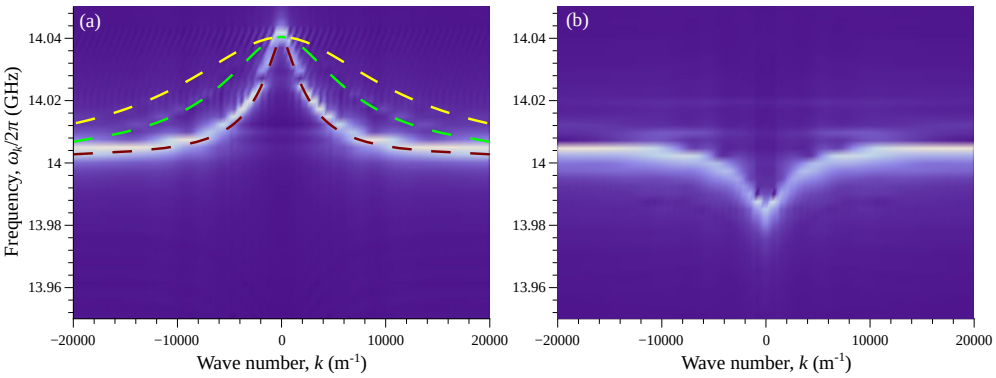

Fig. 4 Spectrum of magnetostatic waves for $M_\mathrm{s} = 2.2\,\mathrm{kA/m}$**. a,** external field along the capillary axis, **b,** external field perpendicular to the capillary axis. Colour maps represent results of micromagnetic simulations, dashed lines in **a** semi-analytical solution for the first three modes with nonzero dynamic magnetic moment.

magnonics [5]. Denoting uncoupled magnon and polariton frequencies as ω_m and ω_p (both k-dependent), respectively, the coupled wave dispersion is expressed as

$$\omega_{1,2} = \frac{\omega_p + \omega_m}{2} \pm \sqrt{\left(\frac{\omega_p - \omega_m}{2}\right)^2 + g^2}\,, \tag{5}$$

where g is the coupling strength between magnon and polariton modes. This coupling can be estimated as [5]:

$$g \simeq \frac{\gamma}{2}\sqrt{\frac{\mu_0 \hbar \omega_p V_m M_\mathrm{s}}{V_p \mu_B}}, \tag{6}$$

where μ_0 is vacuum permeability, μ_B is Bohr magneton, V_m, V_p are volumes of magnon and polariton modes, M_s is the saturation magnetization. This estimate represents the maximum possible coupling estimation, excluding mode overlap efficiency and other factors. For our parameters, we arrive at the estimation around $g/(2\pi) \simeq 250\,\mathrm{MHz}$ for $M_s = 2200\,\mathrm{A/m}$.

The dispersion of the lowest polariton mode $\omega_p(k)$ in a dielectric cylindrical waveguide is linear, $\omega_p(k) = v_p|k_x|$. As follows from Ref. [6], the polariton velocity can be estimated as $v_p \simeq c/(2\sqrt{\epsilon})$, where c is the speed of light and $\epsilon \approx 8$ is the TEMPO dielectric permeability.

2.4 Magnon-polariton pulse propagation

In our case, the magnon-polariton coupling strength is comparable to the magnon linewidth. This makes pulse propagation more involved, since a range of waves with much different group velocities are excited simultaneously due to relatively large linewidth. To check weather our experimental observations are consistent with magnon-polariton physics, we simulate pulse transmission by magnon-polaritons.

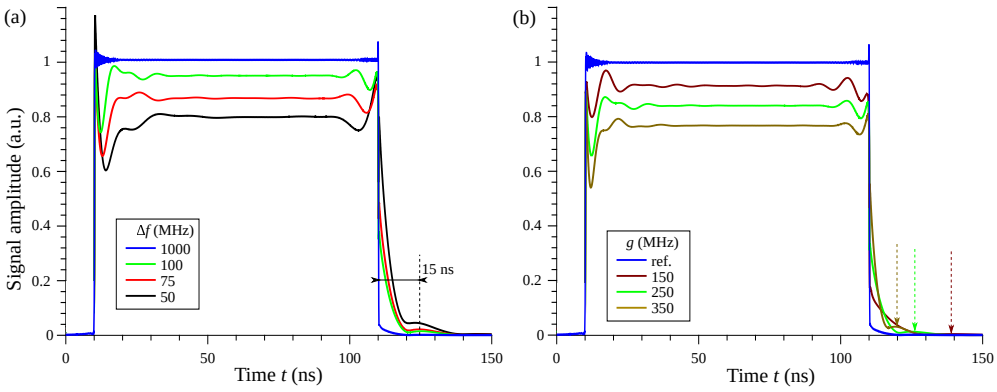

Fig. 5 Simulation of magnon-polariton pulse propagation. Simulations are made for 100 ns pulse (start time is $t_0 = 10$ ns); **a** – in dependence on the offset of the pulse frequency from magnon frequency $\Delta f = (\omega_e - \omega_m)/(2\pi)$ at fixed coupling $g = 2\pi \times 250$ MHz, (b) – in dependence on the coupling strength for fixed $\Delta f = 100$ MHz (except for the reference pulse, calculated at 1 GHz offset). Pulse amplitudes are normalized to different levels for clear visualization. Vertical arrows in (b) denote position of the first subsequent peak in the pulse time trace.

The model is the following. Since the crossing of paramagnon and polariton branches takes place at very low k, we neglect magnon dispersion and set $\omega_m = \omega_H$. Then, for any frequency we get corresponding wave vector $k_j = k_j(\omega)$ and group velocity v_j of the coupled wave using Eq. (5). From the same equation, if change magnon and polaron frequencies to their complex values $\omega_{m,p} \to \tilde{\omega}_{m,p} = \omega_{m,p} - i\Gamma_{m,p}$, which accounts for the damping, we get damping rate of the coupled magnon-polariton wave as $\Gamma_{1,2} = -\mathrm{Im}[\tilde{\omega}_{1,2}]$. Finally, assuming that only magnons are excited by an external harmonic force (this simplification is used since we don't know phase relations between forces acting on magnons and polaritons), we get excitation amplitude $c_j(\omega_e) = -i(\omega_e - \tilde{\omega}_p)/(\Gamma_j(\omega_e - \tilde{\omega}_l))$, where $j = 1, 2$ denotes lower and upper magnon-polariton branches, $l \neq j$ and ω_e is the excitation frequency. The shape of a propagating pulse is given by

$$m(t) = \mathcal{F}^{-1}\left[S_{in}(\omega)\mathrm{sinc}\left(\frac{k_j w}{2}\right) c_j(\omega) e^{ik_j L} e^{-\Gamma_j L/v_j}\right], \tag{7}$$

where $j = 1$ for $\omega > \omega_m$ and $j = 2$ for $\omega < \omega_m$, L is the propagation distance, w is the antenna width, $S_{\mathrm{in}}(\omega)$ is the spectrum of input pulse, and $\mathcal{F}^{-1}$ denotes inverse Fourier transform.

Calculations for the propagation length of 4 mm are summarized in Fig. 5. We set Gilbert damping parameter for TEMPO to $\alpha_G \approx= 0.004$ as follows from EPR linewidth (Fig. 1(e) in the main text), and set 100 times smaller damping for polaritons (calculations require a nonzero value, even if it is very small). In panel (a), the pulse frequency is varying in the vicinity of the magnon-polariton hybridization point and the coupling strength is fixed to the above estimated value of $g/2\pi = 250$ MHz; the curve for $\Delta f = 1000$ MHz serves as a reference for pure polariton transmission.

While the pulse shape is changing somewhat with the pulse frequency, subsidiary peak appears almost at the same delay of 15 ns, similar to the experimental observation. To prove that the delay of subsidiary pulse could serve as a measure of magnon-polariton coupling, we perform calculations for different values of g at a fixed pulse frequency. From Fig. 5(b) it is clear, that the stronger is the coupling, the larger is the amplitude and the shorter is the delay of the subsidiary pulse.

3 Experimental setup

Supplementary Fig. 6 illustrates our experimental dilution refrigerator setup, where the continuous-frequency and pulsed time-resolved propagating spin-wave measurements are conducted. It can be divided into the ^{3}He/^{4}He dilution refrigerator and the excitation/detection electronics.

The cryogenic-free dilution refrigerator system is the *Bluefors-LD250*, which achieves base temperatures below 10 mK at the mixing chamber stage. The sample space possesses a base temperature of about 16 mK. During operation, the sample space heats up to about 50-85 mK in our experiments. Depending on the applied magnetic field, the dilution refrigerator can be operated continuously between the base temperature and about 3.6 K. The input signal (orange input path Supplementary Fig. 6) is feet into the dilution refrigerator using copper wire and a total attenuation of -12 dB, ensuring a good signal-to-noise ratio. As mentioned in the previous section, the TMEPO sample is mounted on a high frequency and placed in the homogeneous field of a superconducting magnet. The output signal (yellow output path Supplementary Fig. 6), uses a combination of superconducting wiring (yellow, 10 mK - 4 K) and copper wiring (orange, 4 K - 297 K) without attenuation.

The excitation/detection unit consists of two options that can be switched. The first one is the excitation and detection of the propagating spin wave in cf-mode, using a 70 GHz vector network analyser (*Anritsu VectorStar MS4647B*), with which we detect the S_{21}-parameters. For the cf-measurements of the 4 mm spaced antennas (see main text), we use an amplification (A in Supplementary Fig. 6) at the output of 20 dB (*nexTec-RF NB00407*, frequency range 12 - 27 GHz). The microwave power at the sample at the input side is about -4 dBm, considering cable losses and attenuation. These experimental conditions are used for EPR measurements and the stripline antenna.

For the pulsed measurement with the 4 mm spaced antennas on the PCB, we modify the excitation/detection setup. As the pulsed microwave source, we use the *Anritsu MG3692C* (S in Supplementary Fig. 6). For the detection (O in Supplementary Fig. 6) we use the *Teledyne HDO6034* oscilloscope, together with a fast detection diode *OMNIspectra Mod20760* and RF-bandpass filter *Mini-Circuits VHF-6010+* (F, D in Supplementary Fig. 6). As we exemplify the pulsed measurement for a selected external magnetic field of 500 mT and the signal would be too weak to be detected with the fast diode/oscilloscope, we add the amplifier *Low Noise Factory LNR4-14C-SV*, reducing the detectable frequency range to about 12 - 16 GHz. However, this increased the measured amplitude in the cf-measurements (compare Fig. 2 and Fig. 3 in main text).

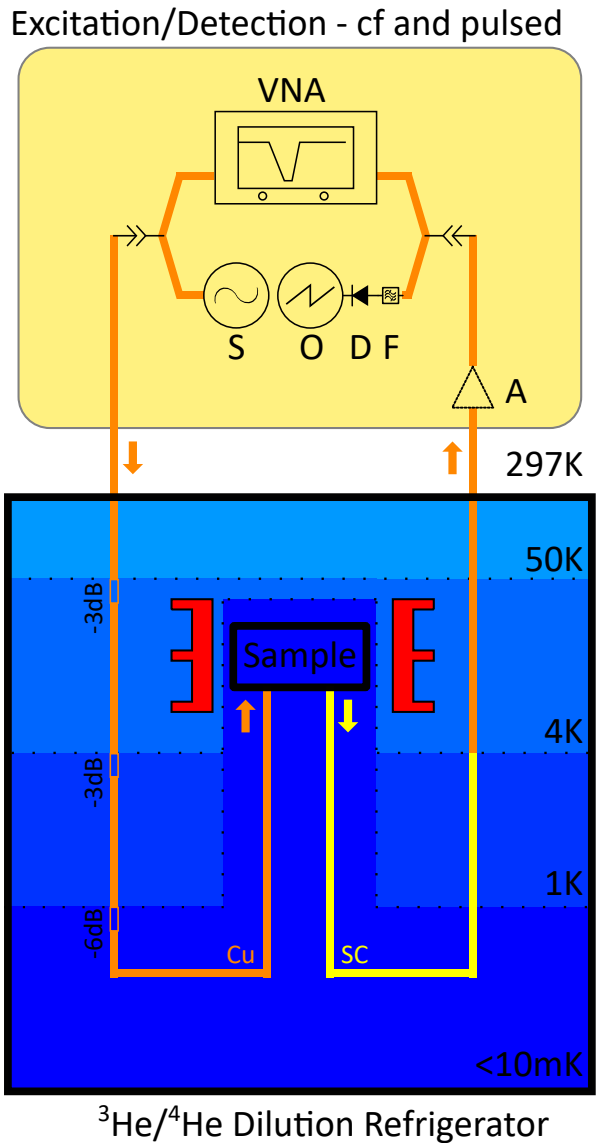

Fig. 6 Schematic of experimental cryogenic setup. The EPR, continuous-frequency and pulsed measurements between millikelvin and Kelvin temperatures are performed in the dilution refrigerator. The setup consists of two major parts: the ^{3}He/^{4}He dilution refrigerator and the excitation/detection electronics.

To demonstrate the pulsed measurement and reference cf-measurement with 8 mm-spaced RF-antennas (compare main text and Supplementary Section 5), we have to add a third amplifier (*nexTec-RF nbl00437*), limiting the frequency range to 12 - 16 GHz, but gaining a total amplification of about +90 dB. Future experiments will

benefit from 4 K-cryo-amplifiers in a high-frequency range, which were unavailable for the present experiments.

4 EPR measurements - Electron Zeeman interaction

As a result of the Zeeman effect, the state energy difference of an electron with $s = 1/2$ in the presence of an external magnetic field is given by

$$\Delta E = g\mu_{\mathrm{B}} B_{\mathrm{ext}}, \tag{8}$$

where μ_{B} is the Bohr magneton, B_{ext} the external applied magnetic field, h the Planck constant, and g the Landé factor. As the energy absorbed by the electron should be the same as the state energy difference ΔE, $\Delta E = hf$, the Supplementary Eq. 8 can be expressed as

$$f = \mu_{\mathrm{B}} B_{\mathrm{ext}} g/h. \tag{9}$$

The observed splitting in the EPR spectra (see Fig.1e main text) may originate from the hyperfine interaction of the unpaired electrons with the nuclei, which seems to increase with decreasing temperature. In the case of one unpaired electron, the spin Hamiltonian can be written as below for the isotropic part of nuclear hyperfine interaction:

$$H = H_{\mathrm{EZ}} - H_{\mathrm{NZ}} - H_{\mathrm{HFS}}, \tag{10}$$

where H_{EZ} represents the electron Zeeman, H_{NZ} the nuclear Zeeman and H_{HFS} the hyperfine interaction. Equation 10 can be re-written as

$$\hat{H} = g\mu_{\mathrm{B}} B_{\mathrm{ext}} S_z - g_{\mathrm{N}}\mu_{\mathrm{N}} \cdot B_{\mathrm{ext}} I_z + h \cdot S \cdot aI, \tag{11}$$

where $S \cdot aI$ describes the Fermi contact interaction, I is the nuclei spin. As μ_{B} is much larger than μ_{N}, Eq. 11 can be simplified to

$$\hat{H} = g\mu_{\mathrm{B}} B_{\mathrm{ext}} S_z + h \cdot S \cdot aI. \tag{12}$$

In literature, e.g. Ref. [7], we find that the hyperfine constant a at room temperature ranges between 1.3 mT and 1.9 mT in both bulk and solution, leading to an expected hyperfine splitting of approximately 43–53 MHz. However, values for bulk TEMPO, particularly for low temperatures, are absent regarding hyperfine constants. For our EPR measurements, we observe a splitting at 3.5 K of approximately 42 MHz, at 750 mK of about 46 MHz, and at 50 mK of approximately 83 MHz, based on the double Lorenzian fit (see Fig. 1d in the main text). The values at 3.5 K and 750 mK are consistent with the literature, and can be explained with the hyperfine interaction. Like the Landé factor, our experimental setup cannot resolve the complete hyperfine tensor. Additionally, the increase in splitting and broadening at 50 mK cannot be fully explained. In the absence of literature values, this is beyond the scope of this manuscript, as we concentrate on demonstrating propagating spin waves below and above the Néel temperature.

5 Propagating paramagnon-polaritons

5.1 Propagating paramagnon-polaritons - additional data

In the main text, we demonstrated the magnetic field-dependent propagation of paramagnons, as an example at 85 mK (see Main Text Figure 2b). In Supplementary Fig. 7 we show magnetic field-dependent AEPSWS (Background corrected real part of part of S'_{21} at different external magnetic fields) over a distance of 4 mm at 3550 mK (above the Néel temperature), for $B_{\parallel}$ (Supplementary Fig. 7a) and $B_{\perp}$ (Supplementary Fig. 7b). We observe a similar behaviour for the parallel applied magnetic field as reported in the main text. However, compared to the millikelvin case, we observe at 3550 mK, that at low magnetic fields, for example at 450 mT, the amplitude remains high. Similar to the millikelvin case, at fields below 300 mT the paramagnon signal vanishes.

These results are corroborated by observations made under a perpendicular applied magnetic field (Supplementary Fig. 7b). However, the magnon signal exhibits a narrower profile than that observed in a parallel applied magnetic field. This suggests that the paramagnon spectrum observed for $B_{\parallel}$ may incorporate modes stemming from the perpendicular excitation direction. Note that, for $B_{\perp}$, our experimental setup restricts our maximum field to 700 mT at a temperature of 3550 mK.

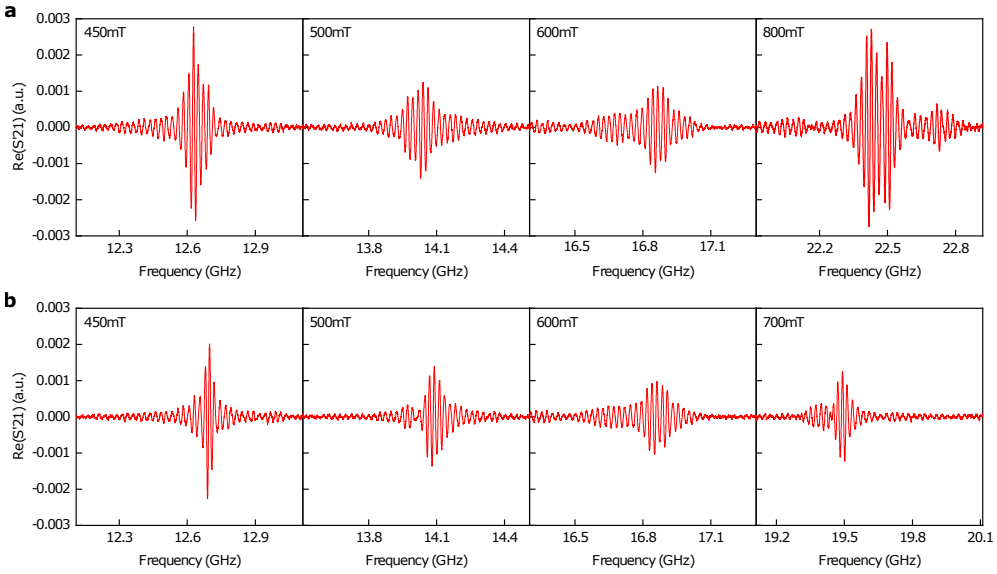

Fig. 7 Magnetic field-dependent AEPSWS of TEMPO for 4 mm antenna spacing at 3550 mK. **a,** Background corrected real part of part of S'_{21} at different external magnetic fields for $B_{\parallel}$. **b,** Background corrected real part of part of S'_{21} at different external magnetic fields for $B_{\perp}$. For more details, see Supplementary Text.

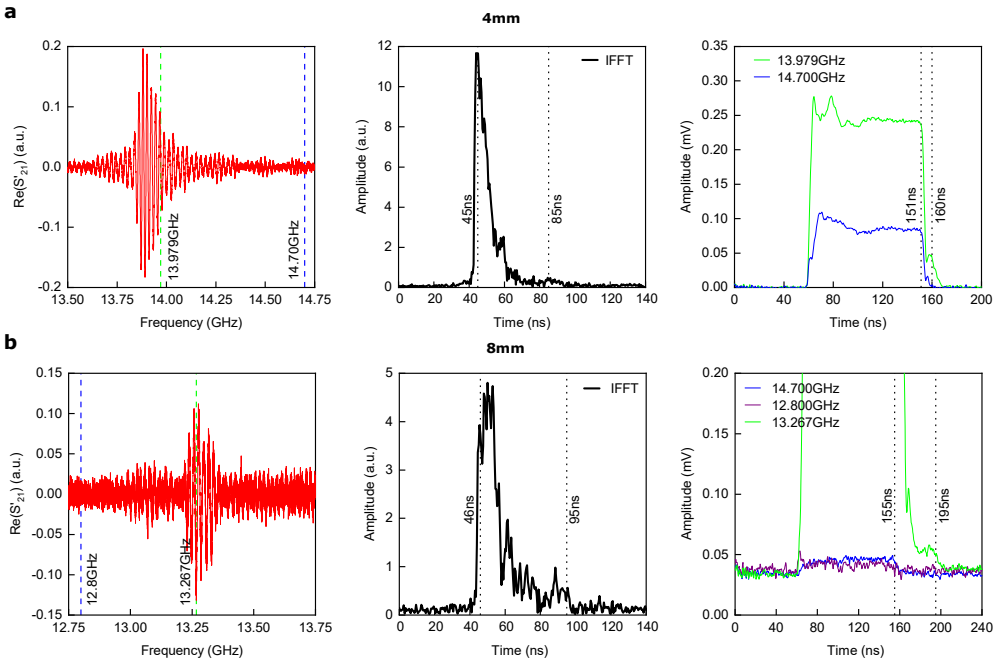

Fig. 8 Comparison time-resolved measurement of 4 mm and 8 mm antenna spacing. **a,** Continuous-frequency reference measurement (real part), IFFT and pulsed measurement for $B_\perp = 500\,\mathrm{mT}$ and 55 mK, at 4 mm antenna spacing, as described in main text. **b,** Continuous-frequency reference measurement (real part), IFFT and pulsed measurement for $B_\perp = 480\,\mathrm{mT}$ and 70 mK, at 8 mm antenna spacing, as described in the main text. In the IFFT the first peak at 46 ns originates from the electromagnetic delay/leakage in the setup. The signal is visible until about 95 ns, resulting in a spin-wave propagation time of about 49 ns. In the pulsed measurement (last graph), we compare the on-resonant (13.267 GHz, green) with two off-resonant (blue, purple) signals. A 100 ns pulse with a repetition rate of 1 ms is applied. Consistent with the IFFT, a propagation time of about 40 ns is found when comparing on-resonant and off-resonant propagation signals, leading to minimum group velocities of about $v_\mathrm{g} \approx 160 - 200\,\mathrm{km/s}$. Compared to the 4 mm measurement, this sets a narrower bound on the group velocity, as the error originating from the setup (rise/fall time) is less critical.

5.2 Comparison of time-resolved measurements

To reinforce the results presented in the main text, which demonstrate the propagation of paramagnons, we include additional data here. Supplementary Fig. 8 illustrates the time-resolved pulsed measurements for antennas spaced 4 mm and 8 mm apart. Panel **a** depicts the same results as in the main text for the 4 mm spaced antennas: reference cf-signal, IFFT, and time-resolved pulsed measurement.

To verify these results, we mount the sample on a PCB (similar to Supplementary Fig. 1) with an antenna spacing of 8 mm (Supplementary Fig. 8, panel b). For these measurements, we had to add an amplifier (see Supplementary Section 2), as the propagation signal is weaker, and in comparison, the visibility of the electromagnetic leakage as well. Thus, our measurement range was limited to a small magnetic field window of $B_\perp = 480\,\mathrm{mT}$, where the cf-measurement and the pulsed measurement were

visible. The first graph in Supplementary Fig. 8b shows the real part the cf-reference measurement of the 8 mm spaced antenna for $B_\perp = 480\,\mathrm{mT}$. The 8 mm measure could be performed at about 70 mK. The IFFT (Supplementary Fig. 8b, second graph) show the first peak at 46 ns, originating from the electromagnetic delay/leakage in the setup, which is consistent with the 4 mm measurement (within the measurement error). The signal is visible until about 95 ns, resulting in a spin-wave propagation time of about 49 ns. In the pulsed measurement (Supplementary Fig. 8b, third graph), we compare the on-resonant (13.267 GHz, green) with two off-resonant signals: 12.8 GHz (blue) and 14.7 GHz. The 14.7 GHz off-resonant signal allows us a good comparison between the leakage signal of the 4 mm and 8 mm measurements. Similar to the 4 mm measurement, a 100 ns pulse with a repetition rate of 1 ms is applied. The difference between the resonant (green) and off-resonant signals (blue, purple) is even more significant than in the 4 mm case, necessitating scaling the resonant signal (green) out of the plot range, to observe the electromagnetic leakage still. The plot is kept in a linear scale to show direct comparison. We find that the on-resonant signal is about 70 times greater than the off-resonant signal. The behaviour of the resonant and off-resonant pulse in the 8 mm spacing was trackable between the 70 mK presented above and 1.5 K. At the same time, the effect was not measurable around 3.5 K, similar to the 4 mm antenna spacing.

At the resonant frequency, additional electromagnetic wave transmission occurs through the nonconductive, ferromagnetically ordered medium. This phenomenon arises from the intersection of the dispersion relations of microwaves and paramagnons, resulting in a photon–magnon hybrid mode. These hybrid excitations propagate through the magnetic medium at the speed of light and are detected simultaneously with the electromagnetic leakage, preceding the arrival of the slower, purely paramagnon signals [8].

This behaviour confirms our previous findings that a propagating paramagnon-polariton signal causes the propagation. Consistent with the IFFT, a propagation time of about 40 ns is observed when comparing on-resonant and off-resonant propagation signals, resulting in minimum group velocities of about $v_\mathrm{g} \approx 160 - 200\,\mathrm{km/s}$ for the slowest propagating paramagnons. The difference between the IFFT and pulsed measurements in estimating the group velocity is smaller in the 8 mm case than in the 4 mm case, as at such high velocities (short delay time), errors from a finite rise/-fall time of the fast diode are less critical. The measurements from the 8 mm samples robustly corroborate our findings from the main text concerning the 4 mm spaced antennas. We observe that the propagation signals originate from the propagation of paramagnons, which are distinctly separable from electromagnetic leakage in both frequency and time domains. This distinction allows us to confidently report similar minimum propagation velocities for the slowest paramagnons within the measurement error margins of about $v_\mathrm{g} \approx 100 - 440\,\mathrm{km/s}$.

Our results demonstrate that the propagation signal can be precisely adjusted by applying an external magnetic field, as our theoretical findings support. These outcomes confirm our initial hypotheses presented in the main text and enhance our understanding of paramagnon dynamics under various experimental conditions.

5.3 Reconstruction of pulse shape

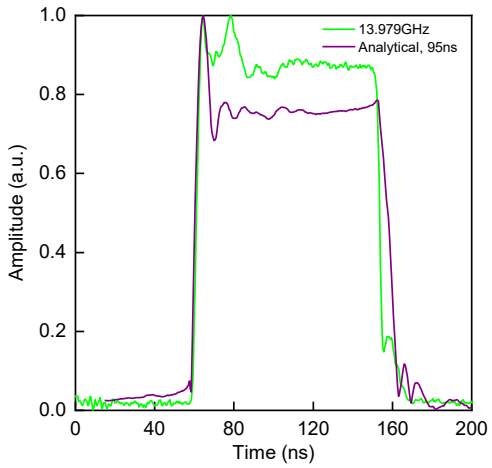

Fig. 9 Comparison time-resolved pulsed measurement with reconstructed analytical solution $\mathbf{B}_\perp = 500\,\mathbf{mT}$, 55 mK The pulsed result with the on-resonant (13.979 GHz, green) signal, from the main text (Fig. 3a, 55 mK), and the analytical results (dark red) show close agreement. To obtain the analytical results, we take Supplementary Eq. 13, convolve it with the measured transmission spectrum (S_{12}) and then Fourier transform it into the time domain. For the analytical result, we use $\tau = 95$ ns, compared to the 100 ns in the experiments. This difference is due to the experimental inaccuracy and the propagation length in the dilution refrigerator. Also, to compare with the experimental results, we have adjusted the time scale of the analytical results to account for propagation delay in the pulsed setup.

In the previous section and main text, we discussed observing the time delay caused by spin waves in pulsed measurements. To support our results, we compared this to the analytical response derived from the continuous-frequency spectrum.

To compare our results, we use the analytical function

$$F(f) = \frac{i}{2\pi(f - f_c)} \exp\left[2\pi i(f - f_c)t_0\right]\left(1 - \exp\left[2\pi i(f - f_c)\tau\right]\right), \tag{13}$$

where f_c represents the carrier frequency of the pulse , t_0 the start time of the pulse, and τ.

Supplementary Fig. 9 compares the pulse results between the on-resonant (13.979 GHz, green), from the main text (Fig. 3b), and the analytical results (dark red). To obtain the analytical results, we take Supplementary Eq. 13, convolve it with the measured transmission spectrum (S_{12}), as described in the main text, and then Fourier transform it into the time domain. As mentioned in the main text, we are using a 100 ns pulse, with a repetition of 1 ms, however, we find that a pulse of about $\tau = 95$ ns approximates the analytical pulse most closely to the measured pulse. This difference can be attributed to experimental inaccuracies in pulse generation and the propagation of this pulse through the dilution refrigerator. Additionally, we have

shifted the analytical pulse to align with the experimental pulse on the rising edge, around 44 ns. We observe that the pulse shape is qualitatively reproduced, and the period of oscillations, between 45 ns to about 100 ns, matches between the analytical and measured pulse. However, the amplitude drop-off is different between the signals.

The reconstruction of the measured pulse confirms that the modulation observed in pulsed measurements originates indeed from the propagating paramagnon-polaritons.

5.4 Group velocity estimation at few-Kelvin temperature

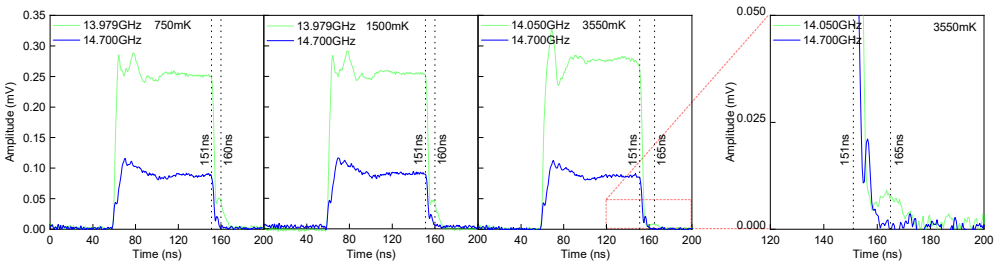

Fig. 10 Pulses measurement with respect to temperature for 4 mm antenna spacing. While the time delay, about 9 ns, thus $\sim$ 440 km/s, between on-resonant (13.979 GHz / 14.050 GHz, green) and off-resonant (14.700 GHz, blue) remains consistent between 55 mK (see Fig. 3c main text) and 750 mK to 1500 mK (here), we observe at 3550 mK a time delay of $\sim 14\,ns$, suggesting 285 km/s (third plot and zoomed plot). However, the signal peak at 165 ns (green) is very weak and remains to be verified in future research. For more details, see the text.

Reconstructing the pulse shape from the previous section enables us to estimate the group velocity even at temperatures of a few Kelvin, where direct pulse measurements produce inconclusive results due to weak measurement signals.

Together with the main text Fig. 3c and Supplementary Fig. 8 (right column) and Fig. 10 we show that the pulsed measurements are consistent from the millikelvin into the low Kelvin (see Fig. 10, 1500 mK) We observe that the time delay between resonant (13.979 GHz, green) and off-resonant excitation (14.700 GHz, blue) remains constant by about 9 ns, leading to a group velocity of about 440 km/s, as stated in the main text. However, we observe that, although the amplitude of the propagating signal (see Fig. 1f and Fig. 2a main text) increases near the Néel temperature, we observe inconclusive results for the pulsed measurements. Supplementary Fig. 10 shows for 3550 mK (third plot and zoomed plot), a small (potential) peak in the on-resonant signal (14.050 GHz, green) at around 165 ns. The tested resonance frequency was shifted, as the resonance shifts between millikelvin and Kelvin temperatures (see Fig. 1f and Fig. 2a main text for temperature comparison). The peak at 165 ns would lead to a time delay of about 14 ns, suggesting a group velocity of about 285 km/s. This value suggests that the group velocity increases closer to the Néel temperature. However, the signal strength in the pulsed measurement around three Kelvin becomes very weak. Thus, we do not report this value in the main text. Currently, it is unclear why we observe such a weak signal at these temperatures for all magnetic orientations and antenna spacings.

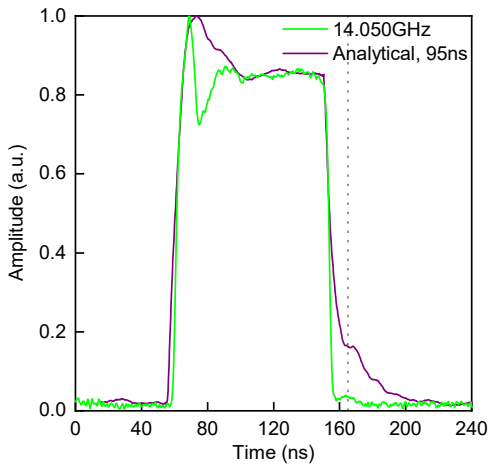

Fig. 11 Comparison time-resolved pulsed measurement with reconstructed analytical solution $\mathbf{B}_\perp = 500\,\mathbf{mT}$, 3550 mK. Although an amplitude difference between the analytically reconstructed pulse (turquoise) and the measured on-resonance pulse (14.050 GHz) on the falling edge, around 165 ns (dashed line), can be observed, the analytical pulse confirms that this edge of the pulse smears out. But a signal at 165 ns seems plausible. For more details, see the text.

One explanation might be different transmission properties of the microwave cables in the dilution refrigerator and an additional decrease in signal-to-noise ratio at Kelvin temperatures. To answer this question in depth will remain for future studies.

However, we take our 3550 mK data (see Fig. 1f and Fig. 2a, main text), and reconstruct the pulse as shown in the previous section. The results are shown in Supplementary Fig. 11, for the analytical reconstruction (turquoise, "Analytical, 95ns") and the on-resonance measured pulse (green, "14.050GHz"). We observe that the rising edge smears out, especially when compared to Supplementary Fig. 9 (turquoise). This behaviour is crucial for understanding our measured data. For comparison, we have marked the 165 ns point (dashed line). Our relative amplitude at this point (green) is lower than the analytical reconstruction would suggest. Thus, our measured signal might be hidden in the background. However, the analytical signal suggests a peak around 165 ns, confirming that the time delay increases to 14 ns, leading to a group velocity of about 285 km/s. Future measurements will have to investigate the physical mechanism for the pulse shape change between millikelvin and Kelvin temperatures.

References

[1] Barak, J., Huang, M.X., Bhagat, S.M.: Electron paramagnetic resonance study of gadolinium–gallium–garnet. Journal of Applied Physics **71**(2), 849–853 (1992) https://doi.org/10.1063/1.351305

[2] Arias, R., Mills, D.L.: Theory of spin excitations and the microwave response of cylindrical ferromagnetic nanowires. Physical Review B **63**(13), 134439 (2001) https://doi.org/10.1103/PhysRevB.63.134439

[3] Das, T.K., Cottam, M.G.: Magnetostatic modes in nanometer-sized ferromagnetic and antiferromagnetic tubes. Surface Review and Letters **14**(03), 471–480 (2007) https://doi.org/10.1142/S0218625X07009505

[4] Vansteenkiste, A., Leliaert, J., Dvornik, M., Helsen, M., Garcia-Sanchez, F., Van Waeyenberge, B.: The design and verification of MuMax3. AIP Advances **4**, 107133 (2014) https://doi.org/10.1063/1.4899186

[5] Pfirrmann, M., Boventer, I., Schneider, A., Wolz, T., Kläui, M., Ustinov, A.V., Weides, M.: Magnons at low excitations: Observation of incoherent coupling to a bath of two-level systems. Physical Review Research **1**(3), 032023 (2019) https://doi.org/10.1103/PhysRevResearch.1.032023

[6] Shevgaonkar, R.K.: Electromagnetic Waves. Electrical & Electronic Engineering. McGraw-Hill Education (India) Pvt Limited, New Delhi (2005)

[7] Kobayashi, H., Ueda, T., Miyakubo, K., Toyoda, J., Eguchi, T., Tani, A.: Preparation and characterization of a new inclusion compound with a 1D molecular arrangement of organic radicals using a one-dimensional organic homogeneous nanochannel template. Journal of Materials Chemistry **15**(8), 872 (2005) https://doi.org/10.1039/b412407c

[8] Gurevich, A.G., Melkov, G.A.: Magnetization Oscillations and Waves, pp. 96–104. CRC Press, Boca Raton (1996). Chap. 4.2